Earthq Eng & Eng Vib (2023) 22: 211-223 **DOI**: https://doi.org/10.1007/s11803-023-2162-3

An extended multiple-support response spectrum method incorporating fluid-structure interaction for seismic analysis of deep-water bridges

Wu Kun[1†], Li Ning[2‡] and Li Zhongxian[2‡]

1. *School of Transportation Science and Engineering, Civil Aviation University of China, Tianjin 300300, China*

2. *Key Laboratory of Coast Civil Structures Safety of the Ministry of Education, Tianjin University, Tianjin 300350, China*

Abstract: The effects of ground motion spatial variability (GMSV) or fluid-structure interaction (FSI) on the seismic responses of deep-water bridges have been extensively examined. However, there are few studies on the seismic performance of bridges considering GMSV and FSI effects simultaneously. In this study, the original multiple-support response spectrum (MSRS) method is extended to consider FSI effect for seismic analysis of deep-water bridges. The solution of hydrodynamic pressure on a pier is obtained using the radiation wave theory, and the FSI-MSRS formulation is derived according to the random vibration theory. The influence of FSI effect on the related coefficients is analyzed. A five-span steel-concrete continuous beam bridge is adopted to conduct the numerical simulations. Different load conditions are designed to investigate the variation of the bridge responses when considering the GMSV and FSI effects. The results indicate that the incoherence effect and wave passage effect decrease the bridge responses with a maximum percentage of 86%, while the FSI effect increases the responses with a maximum percentage of 26%. The GMSV and FSI effects should be included in the seismic design of deep-water bridges.

Keywords: response spectrum method; seismic response of bridge; ground motion spatial variability; fluid-structure interaction; rdiation wave theory

1 Introduction

Deep-water bridges are typically located in areas with severe and complex conditions, and susceptible to the excitation of various loads, such as earthquake, wave and sea current, etc., during its service period. (Ding *et al*., 2018; Miao *et al*., 2021). Many studies have been conducted on the ground motion spatial variability (GMSV) (Der Kiureghian and Neuenhofer, 1992) and fluid-structure interaction (FSI) (Penzien and Kaul, 1972), which significantly affects the seismic performance of deep-water bridges. The main sources of GMSV effect are loss in the coherence of the seismic waves with distance, called the incoherence effect, difference in the arrival time of the seismic waves at different supports, called the wave passage effect, and difference in the soil conditions at each support, called the local site effect. The main forms of FSI effect are earthquake induced hydrodynamic pressure and wave forces on substructures of the bridge, such as piers, abutments, and piles. A suitable seismic-resistant design for extended bridges should consider the GMSV and FSI effects (Meng *et al*., 2018).

The characteristics and responses of structures subjected to multi-support ground motions have been studied by many researchers. The frequently-used methods are time history analysis method (Yang *et al*., 2002; Li *et al*., 2010; Abdel *et al*., 2011; Mirzabozorg *et al*., 2012; Hu *et al*., 2012; Wang *et al*., 2018; Zheng *et al*., 2019; Mohammadnezhad *et al*., 2019), experimental method (Li *et al*., 2015; Koufoudi *et al*., 2018; Zhang *et al*., 2020), response spectrum method (Der Kiureghian and Neuenhofer, 1992; Yu and Zhou, 2008; Konakli and Der Kiureghian, 2011; Wang and Der Kiureghian, 2014; Nazarov and Poznyak, 2018), and random vibration method (Dumanogluid and Soyluk, 2003; Soyluk and Dumanoglu, 2004; Lin *et al*., 2005; Bi *et al*., 2010). Hu *et al*. (2012) proposed a time history analysis simulation method of ground motions considering the GMSV effect for large span bridges. Li *et al*. (2015) carried out shaking table tests to explore the influence of local site effect and wave passage effect on the responses of a curved bridge. Der Kiureghian and Neuenhofer (1992) presented a multiple-support response spectrum (MSRS) method to study the seismic performance of structures

Correspondence to: Li Ning, Key Laboratory of Coast Civil Structures Safety of the Ministry of Education, Tianjin University, Tianjin 300350, China
Tel: +86-22-27403768
E-mail: neallee@tju.edu.cn

†Lecturer; ‡Professor

Supported by: National Natural Science Foundation of China under Grant Nos. 51427901 and 51678407, Tianjin Municipal Education Commission under Grant No. 2021KJ055, and Fundamental Research Funds for the Central Universities of China under Grant No. 2000560616

Received July 15, 2021; **Accepted** July 28, 2022

considering the GMSV effect. The MSRS method was then applied to investigate the influence of GMSV effect on responses of the Golden Gate Bridge (Nakanura *et al*., 1993). Subsequently, Konakli and Der Kiureghian (2011) extended the MSRS method to include the quasi-static contribution of high-order modes that is truncated in the original MSRS method. Wang and Der Kiureghian (2014) developed the MSRS method in conjunction with load-dependent Ritz (LDR) and proposed the LDR-MSRS method. The accuracy of the method is not worse than the extended MSRS method (Konakli and Der Kiureghian, 2011) and better than the original MSRS method (Der Kiureghian and Neuenhofer, 1992). Dumanogluid and Soyluk (2003), Wang and Der Kiureghian (2014), and Soyluk and Dumanoglu (2004) applied response spectrum method and random vibration method to analyze the dynamic responses of a cable-stayed bridge considering the GMSV effect. A common conclusion in the above studies is that the GMSV effect is essential for the seismic analysis of a bridge.

The responses of bridges subjected to FSI effect have also been studied by many researchers with numerical method and experimental methods. Wang *et al*. (2011) established a finite element model of bridge piers to study the variation of the seismic response when considering FSI effect. The results indicated that the FSI effect clearly increased the internal force and the displacement of the pier. Li and Di (2011) modeled a cable-stayed aqueduct bridge using finite element software ANSYS (Nakasone *et al*., 2006) to investigate its dynamic characteristics and the modal information with and without water was compared in detail. Song *et al.* (2013) proposed a simplified method to calculate the earthquake induced hydrodynamic force on slender structures. The responses of the structure subjected to FSI effect were explored, which was compared with that obtained by shaking table tests and numerical simulation. Meng *et al.* (2018) analyzed the displacement and internal forces of a cable-stayed bridge considering wind and wave combined excitation. Wei *et al*. (2013) carried out numerical analysis and experimental studies to examine the influence of FSI effect on the dynamic characteristics of pile foundations. Ding *et al*. (2018) conducted shaking table tests on a rubber pier to observe the dynamic response under earthquake, wave, and current combined excitation. The results indicated that the earthquake, wave, and current combined excitation should be considered in design of deep-water bridge.

However, due to the different requirements of an actual structural design and academic studies, these two effects typically are separately studied. There are a few methods to investigate the seismic responses of deep-water bridges considering the GMSV and FSI effects simultaneously.

In this study, the MSRS method proposed by Der Kiureghian and Neuenhofer (1992) is extended to consider the GMSV and FSI effects simultaneously, which is called the FSI-MSRS method. The earthquake induced hydrodynamic force exerted on the pier is introduced into the kinetic governing equations of bridges, which is calculated with the radiation wave theory. Then, the proposed method is used for the analysis of a five-span steel-concrete continuous beam bridge modeled in OpenSees software. The influence of the FSI effect on the related coefficients is investigated. Finally, the variation of the responses of the bridge is explored considering the FSI and GMSV effect. The results indicate that the proposed FSI-MSRS method can be used to study the dynamic responses of bridges considering the GMSV and FSI effect simultaneously.

2 Multiple-support response spectrum method incorporating fluid–structure interaction (FSI-MSRS method)

2.1 Solution for hydrodynamic pressure

The radiation wave theory and Morison equation method are the two major methods for calculation of earthquake induced hydrodynamic forces on structures. The Morison equation (Morison *et al*., 1950; Penzien and Kaul, 1972; Cai *et al*., 2003; Veletsos *et al*., 2010; Yuan and Huang, 2010; Li *et al*., 2019) is suitable for structures of small diameter, which is a semi-empirical formula. The radiation wave theory (Wepf *et al*., 1988; Chopra and Goyal, 1991; Sun and Nogami, 1991; Avilés and Li, 2001; Li and Yang, 2013) solves the hydrodynamic forces on large piers. It takes water velocity potential or hydrodynamic pressure as the basic variable, and combines free surface boundary, bottom reflection boundary, water-structure boundary, and Sommerfeld radiation condition to establish the hydrodynamic pressure solution. The key point is to choose an appropriate method for separation of variables to obtain the water velocity potential.

The radiation wave theory is adopted to deduce the hydrodynamic forces as it has rigorous theory and can apply to any structures. As shown in Fig. 1, the water velocity potential of a circular pier is set in plural form (Li and Yang, 2013).

$$\Phi(r,\theta,z,t)=\varphi(r,\theta,z)\mathrm{e}^{\mathrm{i}\omega t} \tag{1}$$

where r, θ, and z are the coordinates in the cylindrical coordinate system, and $\varphi(r, \theta, z)$ refers to the divisor of the velocity potential. The governing equation of water can be obtained.

$$\frac{\partial^2\Phi}{\partial r^2}+\frac{1}{r}\frac{\partial\Phi}{\partial r}+\frac{1}{r^2}\frac{\partial^2\Phi}{\partial\theta^2}+\frac{\partial^2\Phi}{\partial z^2}+K^2\Phi=0 \tag{2}$$

where K denotes the bulk modulus of water, and $K\rightarrow 0$ when ignoring the compressibility of water.

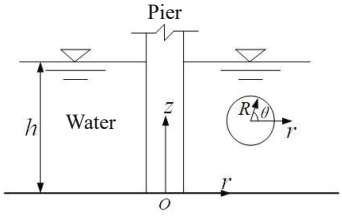

Fig. 1 Diagram of a pier submerged in water

To solve Eq. (2), variables in the water velocity potential is separated using Trefftz functions (Sun and Nogami, 1991).

$$\varphi(r,\theta,z)=\sum_{m=1}^{\infty}\sum_{n=1}^{\infty}R_{mn}(r)\Theta_n(\theta)Z_m(z) \tag{3}$$

The water velocity potential should satisfy the following boundary conditions:

1) water-pier interface boundary condition

$$\frac{\partial \Phi}{\partial r}=\frac{\partial X}{\partial r}\cos\theta,\ r=R,\ -h<z<0 \tag{4}$$

2) free-surface boundary condition

$$\frac{\partial \Phi}{\partial z}-\frac{\omega^2}{g}\Phi=0,\ z=0 \tag{5}$$

3) bottom water boundary condition

$$\frac{\partial \Phi}{\partial z}=0,\ z=-h \tag{6}$$

4) Sommerfeld radiation condition

$$\lim_{r\to\infty}\sqrt{r}\left(\frac{\partial \Phi}{\partial r}-\mathrm{i}k\Phi\right)=0 \tag{7}$$

where h is the water depth, R is the radius of pier, k is the wavenumber, and $X(z, t)$ is the absolute displacement of the pier under ground motion.

Substituting the water velocity potential into Eqs. (4)–(8) and Eq. (2), the hydrodynamic force on pier can be obtained.

$$P=-(\boldsymbol{M}^1x_{\mathrm{g}}''+\boldsymbol{M}^2x'') \tag{8}$$

$$m_{ii}^1=-2\pi W\rho\int_{\Gamma_i}\left\{\frac{\sinh(k_0h)H_1(k_0W)\cosh(k_0z)}{k_0^2\left(h+\sigma^{-1}\sinh^2(k_0h)\right)H_1'(k_0W)}+\sum_{m=1}^{\infty}\frac{\sinh(k_mh)K_1(k_mW)\cosh(k_mz)}{k_m^2\left(h-\sigma^{-1}\sin^2(k_mh)\right)K_1'(k_mW)}\right\}\mathrm{d}z \tag{9}$$

$$m_{ij}^2=-2\pi W\rho\int_{\Gamma_i}\left\{\frac{\cosh(k_0z_j)L_jH_1(k_0W)\cosh(k_0z)}{k_0\left(h+\sigma^{-1}\sinh^2(k_0h)\right)H_1'(k_0W)}+\sum_{m=1}^{\infty}\frac{\cosh(k_mz_j)K_1(k_mW)\cosh(k_mz)}{k_m\left(h-\sigma^{-1}\sin^2(k_mh)\right)K_1'(k_mW)}\right\}\mathrm{d}z \tag{10}$$

where h is the water depth, W is the width of the upstream face, x_{g}'' is the ground acceleration, x'' is the relative acceleration at the node; $\boldsymbol{M}^1$ is a diagonal matrix with element of m_{ii}^1 that represents the added mass matrix caused by the rigid body motion of the pier, $\boldsymbol{M}^2$ is a diagonal matrix with element of m_{ij}^2 that represents the added mass matrix caused by the elastic vibration of the pier; k_0 and k_m are the wave numbers with $k_m=(2m\text{-}1)\pi/(2h)$; $H_1(\cdot)$ is the second type of the first-order Hankel function, $K_1(\cdot)$ is the modified second type of the first-order Bessel function; $\sigma=\omega^2/\mathrm{g}$, ω is the circular frequency of the ground motion, g is the gravity acceleration; z_j is the height of node j along the pier, Γ_i is the integrating range of node i, and superscript′ denotes the derivative.

For a pier with a rectangular cross section, Eq. (12) (Huang, 2011) is used to calculate its hydrodynamic added mass, where the conversion coefficient is fitted with test results.

$$M_{\mathrm{r}}=K_{\mathrm{c}}M_{\mathrm{c}} \tag{11}$$

$$K_{\mathrm{c}}=0.94732+\frac{2.59648}{1+\left(\frac{D/B}{0.09516}\right)^{0.54638}} \tag{12}$$

where M_{r} and M_{c} are the hydrodynamic added mass of rectangular and circular piers, respectively, K_{c} is the conversion coefficient, and D and B are the length and width of cross section of the pier.

2.2 FSI-MSRS formulation

2.2.1 Governing equations

The governing equations of a linear structural system under multi-support ground motions can be expressed as (Der Kiureghian and Neuenhofer, 1992):

$$\begin{bmatrix}\boldsymbol{M} & \boldsymbol{M}_{\mathrm{c}}\\ \boldsymbol{M}_{\mathrm{c}}^{\mathrm{T}} & \boldsymbol{M}_{\mathrm{g}}\end{bmatrix}\begin{Bmatrix}\boldsymbol{x}''\\ \boldsymbol{u}''\end{Bmatrix}+\begin{bmatrix}\boldsymbol{C} & \boldsymbol{C}_{\mathrm{c}}\\ \boldsymbol{C}_{\mathrm{c}}^{\mathrm{T}} & \boldsymbol{C}_{\mathrm{g}}\end{bmatrix}\begin{Bmatrix}\boldsymbol{x}'\\ \boldsymbol{u}'\end{Bmatrix}+\begin{bmatrix}\boldsymbol{K} & \boldsymbol{K}_{\mathrm{c}}\\ \boldsymbol{K}_{\mathrm{c}}^{\mathrm{T}} & \boldsymbol{K}_{\mathrm{g}}\end{bmatrix}\begin{Bmatrix}\boldsymbol{x}\\ \boldsymbol{u}\end{Bmatrix}=\begin{Bmatrix}\boldsymbol{P}\\ \boldsymbol{F}\end{Bmatrix} \tag{13}$$

where $\boldsymbol{x}=[x_1, \cdots, x_n]^{\mathrm{T}}$ denotes the absolute displacements of the unconstrained DOFs; $\boldsymbol{u}=[u_1, \cdots, u_m]^{\mathrm{T}}$ denotes the given displacements at support DOFs; $\boldsymbol{M}$, $\boldsymbol{C}$, and $\boldsymbol{K}$ are

the $n\times n$ matrices of mass, damping, and stiffness related to the unconstrained DOFs; $\boldsymbol{M}_g$, $\boldsymbol{C}_g$, and $\boldsymbol{K}_g$ are the $m\times m$ matrices related to the support DOFs; $\boldsymbol{M}_c$, $\boldsymbol{C}_c$, and $\boldsymbol{K}_c$ are the $n\times m$ coupling matrices related to unconstrained DOFs and support DOFs; $\boldsymbol{P}$ is the forces acting on the unconstrained DOFs that includes the hydrodynamic forces at the underwater nodes of the pier as given by Eq. (9); and $\boldsymbol{F}$ is the m-vector of the reacting forces at the support DOFs.

The absolute displacement vector $\boldsymbol{x}$ consists of pseudo-static displacement and dynamic displacement, $\boldsymbol{x}=\boldsymbol{x}_s+\boldsymbol{x}_d$. The pseudo-static displacement ($\boldsymbol{x}_s$) can be calculated with Eq. (14), $\boldsymbol{x}_s=\boldsymbol{R}\boldsymbol{u}$, where $\boldsymbol{R}=-\boldsymbol{K}^{-1}\boldsymbol{K}_c$ is the influence matrix. Substituting the pseudo-static displacement into Eq. (14) and neglecting the term of damping on the right of the equation, the dynamic displacement of the structure with lumped mass ($\boldsymbol{M}_c = 0$) is obtained.

$$\left(\boldsymbol{M}+\boldsymbol{M}^2\right)\boldsymbol{x}_d''+\boldsymbol{C}\boldsymbol{x}_d'+\boldsymbol{K}\boldsymbol{x}^d=-\left(\boldsymbol{M}+\boldsymbol{M}^1\right)\boldsymbol{R}\boldsymbol{u}'' \tag{14}$$

Assuming classical damping, $\boldsymbol{\Phi}=[\boldsymbol{\varphi}_1\cdots\boldsymbol{\varphi}_n]$ represents the modal matrix of structure, ω_i represents the natural vibration frequency, and ζ_i represents modal damping ratio. The total displacements at the unconstrained DOFs can be described as Eq. (16).

$$\boldsymbol{x}(t)=\sum_{k=1}^{m}\boldsymbol{r}_k u_k(t)+\sum_{k=1}^{m}\sum_{i=1}^{n}\boldsymbol{\phi}_i\beta_{ki}s_{ki}(t) \tag{15}$$

$$\beta_{ki}=-\frac{\boldsymbol{\phi}_i^{\mathrm{T}}(\boldsymbol{M}+\boldsymbol{M}^1)\boldsymbol{r}_k}{\boldsymbol{\phi}_i^{\mathrm{T}}(\boldsymbol{M}+\boldsymbol{M}^2)\boldsymbol{\phi}_i} \tag{16}$$

$$s_{ki}''+2\xi_i\omega_i s_{ki}'+\omega_i^2 s_{ki}=-u_k''(t) \tag{17}$$

where β_{ki} is the modal participation factor related with mode i and support DOF k, $s_{ki}(t)$ is the normalized response of mode i under the kth support motion. The first term in Eq. (15) is the pseudo-static displacement caused by the differential displacements of supports. The second term is the dynamic displacement superposed by the modal contributions.

A specific response, $z(t)$, such as the bending moment or shearing force, is calculated by Eq. (18).

$$z(t)=\sum_{k=1}^{m}a_k u_k(t)+\sum_{k=1}^{m}\sum_{i=1}^{n}b_{ki}s_{ki}(t) \tag{18}$$

$$a_k=q_{u,k}+\boldsymbol{q}_x^{\mathrm{T}}\boldsymbol{r}_k \tag{19}$$

$$b_{ki}=\boldsymbol{q}_x^{\mathrm{T}}\boldsymbol{\phi}_i\beta_{ki} \tag{20}$$

where $\boldsymbol{q}$ denotes the response transfer vector that is calculated with properties of the structure; a_k is the value of responses to solve when the structure is imposed unit displacement at kth support DOF and other support DOFs remain still; and b_{ki} is the effective modal participation factor.

Based on the stationary random vibration theory, the mean of the peak of the specific response, $z(t)$, can be expressed by Eq. (21).

$$E(\max|z(t)|)\approx \left[\sum_{k=1}^{m}\sum_{l=1}^{m}a_k a_l\rho_{u_k u_l}u_{k,\max}u_{l,\max}+2\sum_{k=1}^{m}\sum_{l=1}^{m}\sum_{j=1}^{n}a_k b_{lj}\rho_{u_k s_{lj}}D_l(\omega_j,\xi_j)+\sum_{k=1}^{m}\sum_{l=1}^{m}\sum_{i=1}^{n}\sum_{j=1}^{n}b_{ki}b_{lj}\rho_{s_{ki}s_{lj}}D_k(\omega_i,\xi_i)D_l(\omega_j,\xi_j)\right]^{0.5} \tag{21}$$

where $u_{k,\max}$ is the mean peak of displacement of kth support, $D_k(\omega_i, \xi_i)$ is the value of the displacement response spectrum for kth support motion of modal frequency ω_i and damping ratio ξ_i, ρ_{ukul} is the cross-correlation coefficient between the displacements of kth and lth support, ρ_{ukslj} is the cross-correlation coefficient between the displacement of kth support and response of mode j to the lth support motion, and ρ_{skislj} is the cross-correlation coefficient between the responses of modes i and j to the kth and lth support motions, respectively.

Equation (21) is the proposed FSI-MSRS method for seismic analysis of bridges in deep water considering the GMSV and FSI effects simultaneously. The coefficient a_k is calculated with the finite element model of the structure under unit displacement at kth support DOF, and the coefficient b_{ki} is calculated with the structure under a load of $\phi_i\beta_{ki}$. The $u_{k,\max}$ and $D_k(\omega_i, \xi_i)$ are obtained according to the displacement response spectrum at each support. The three cross-correlation coefficients and the final response are calculated by a custom-made program for the FSI-MSRS method.

In addition, Eq. (15) indicates that the hydrodynamic added mass caused by the elastic vibration $\boldsymbol{M}^2$ is part of the inertia force on the left of the equation and hydrodynamic added mass caused by the rigid vibration $\boldsymbol{M}^1$ contributes to the term of external force on the right of the equation. To consider the FSI effect, the $\boldsymbol{M}^2$ is set at nodes of piers in water to obtain the modal information. The $\boldsymbol{M}^1$ and $\boldsymbol{M}^2$ are added to the mass matrix of the model to calculated the coefficients in Eq. (21). Compared with the original MSRS (Der Kiureghian and Neuenhofer, 1992), the largest difference in the FSI-MSRS method is the addition of the hydrodynamic force in the governing equation, which finally changes the values of b_{ki}, $D_k(\omega_i, \xi_i)$, ρ_{ukslj}, and ρ_{skislj} that will be discussed in Section 4.

2.2.2 Coherency function

For two different support motions, the coherency function $\gamma_{kl}(\omega)$ is the cross-PSD between the two motions divided by the auto-PSDs of the two motions.

Table 1 Results of responses

Responses	Results by FSI-MSRS	Results by Der Kiureghian and Neuenhofer (1992)	Error (%)
1	8.47	7.78	8.9
2	8.32	7.73	7.6
3	49.4	45.4	8.8
4	215	198	8.6
5	194	181	7.2

Table 2 Parameters of the lead rubber bearings

Terms	Values
Size (mm × mm)	1320×1390
Vertical bearing capacity (kN)	19000
Yield force of the lead (kN)	739
Maximum horizontal displacement (mm)	200
Vertical stiffness before yielding (kN/mm)	27.8
Shear modulus (MPa)	0.8

In this study, the coherency function in Der Kiureghian and Neuenhofer (1992) was adopted.

$$\gamma_{kl} = \exp(-(\frac{\alpha\omega d_{kl}}{v_s})^2)\exp(\mathrm{i}\frac{\omega d_{kl}^L}{v_{app}}) \tag{22}$$

where α is the incoherence factor, d_{kl} is the distance between supports k and l, d_{kl}^L is the projected distance between supports k and l along the propagation direction of the seismic wave, v_s denotes the shear wave velocity of the soil, and v_{app} denotes the surface apparent wave velocity. As shown in Eq. (22), the former part on the right represents the incoherence effect, and the later part on the right represents the wave passage effect.

2.2.3 Verification

The two-span continuous beam in Der Kiureghian and Neuenhofer (1992) is adopted to verify the FSI-MSRS method, which is modeled by OpenSees with uniform stiffness and mass. More information on the model and ground motion is given by Der Kiureghian and Neuenhofer (1992). The results of case 4 are obtained for the validation that the incoherence effect and wave passage effect are included with v_{app}=400 m/s and v_s/α=600 m/s. The responses of the mid-span displacement u_1 and u_2, the bending moment M at the middle support, and the shearing force V_1 and V_2 at both sides of the middle support are calculated. The responses are managed to be dimensionless with $\boldsymbol{z}=(z_1\ z_2\ z_3\ z_4\ z_5)=10^3\times(u_1/L\ u_2/L\ LM/EI\ L^2V_1/EI\ L^2V_2/EI)$, where L, E, and I are the length of span, elasticity modulus, and moment of inertia of the cross section, respectively. The results are listed in Table 1. It can be found that the errors between results calculated by the FSI-MSRS method and in Der Kiureghian and Neuenhofer (1992) are less than 10%, which may be caused by the small differences in the numerical model of the structure, integration method for the calculation of three cross-correlation coefficients, etc. Therefore, the proposed FSI-MSRS method is verified to be effective and correct through the comparison.

3 Bridge model and ground motions

3.1 Bridge model

The 5 m × 85 m steel-concrete continuous beam bridge of the non-navigable bridges of the Hong Kong–Zhuhai–Macao Bridge is used to study the influence of GMSV and FSI effects on the dynamic responses of the bridge. The layout, and cross sections of the pier and girder, is shown in Fig. 2. OpenSees (Gu and Huang, 2017) is adopted to establish the finite element model of the structure. The girder consists of elastic beam-column elements, and the piers consist of displacement-based beam-column elements. The fiber element in OpenSees is used to build the cross section of the pier with different fibers to simulate the rebar and concrete respectively, which can obviously improve the computational efficiency. The “Steel02” in OpenSees is used to model the rebar, and the “Concrete02” is used to model the concrete, where the strengthening of hooping is considered for the core concrete.

Two lead rubber bearings are installed between the piers and each box girder, which is modeled with six springs at different DOFs. The parameters of lead rubber bearings are listed in Table 2. The stiffness of springs along the X and Y directions is calculated with shear modulus in Table 2 and that along the Z direction is calculated with the vertical stiffness before yielding. The stiffness of springs at rotational DOF of the X direction is calculated with the vertical stiffness before yielding and distance between the two bearings, and that of the Y and Z directions is assumed to be free and fixed, respectively.

Moreover, the pile foundation is used in the real bridge that is not considered in the 3D model for simplification. As the constraint of pile foundation on the pier is not completely rigid, the bottom of the pier is assumed to be semi-rigid with six springs at different

DOFs to simulate the real condition. The stiffness of the springs is set to obtain reasonable natural vibration frequencies and modal shape of the bridge.

The modal analysis of the bridge is conducted with OpenSees. Figure 3 givens the first eight natural vibration frequencies and corresponding modal shapes. In addition, all the modes are assumed with a 5% damping ratio.

3.2 Ground motions

As shown in Fig. 2, the length of the cross section of the pier along the transverse direction of the bridge is 2.75 times larger than that along the longitudinal direction. Then the longitudinal hydrodynamic force on the pier is much larger than the transverse hydrodynamic force according to Eq. (9). Therefore, the response of bridge under ground motion in the *X*-direction is investigated. A filtered white noise is used to excite the bridge at the supports, where the PSD is calculated by the modified Kanai-Tajimi model (Clough and Penzien, 1975).

$$G_{u_k''u_k''}(\omega) = G_{kk}\frac{\omega_{fk}^4 + 4\zeta_{fk}^2\omega_{fk}^2\omega^2}{(\omega_{fk}^2-\omega^2)^2 + 4\zeta_{fk}^2\omega_{fk}^2\omega^2}\frac{\omega^4}{(\omega_{gk}^2-\omega^2)^2 + 4\zeta_{gk}^2\omega_{gk}^2\omega^2} \tag{23}$$

where G_{kk} is a scale factor, ω_{fk} and ζ_{fk} are the filter parameters that represent the dominant frequency and damping ratio of the soil, respectively, and ω_{gk} and ζ_{gk} are the parameters of the second filter to ensure a finite power for the ground displacement.

The values, G_{kk} = 0.00856 m^2/s^3, ω_{fk} = 13.491 rad/s, ζ_{fk} = 0.822, ω_{gk} = 0.154 rad/s, and ζ_{gk} = 1.140 are chosen to represent M_s 7.0 earthquakes occurring in the medium-soft soil. All the support motions are assumed to have the same auto-PSD and the cross-PSD is calculated by the coherency function with different parameters. The values of v_s/α are 40 m/s, 600 m/s, 2000 m/s, and infinity to examine the incoherence effect, where infinity means no incoherence effect. The values of v_{app} are 40 m/s, 400 m/s, 2000 m/s, and infinity to study the wave passage effect, where infinity means no wave passage effect. The water depth at the side pier of the bridge (h) are 0, 10 m, 20 m, and 30 m to investigate the FSI effect.

As limited by the space, the local site effect is not considered in this study. It is convenient to investigate the influence of the local site effect by changing the values of coefficients in Eq. (23).

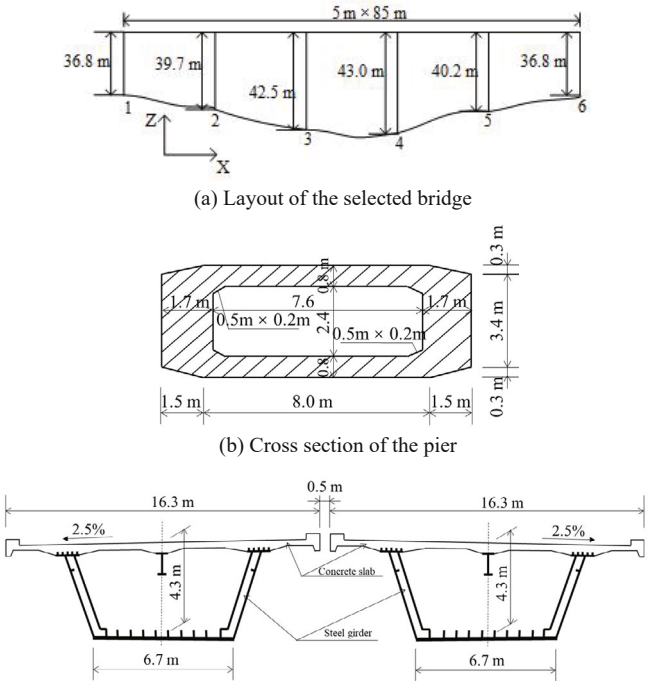

(a) Layout of the selected bridge

(b) Cross section of the pier

(c) Cross section of the girder

Fig. 2 Bridge model

4 Influence of FSI effect on the coefficients

Compared with the original MSRS, the values of b_{ki}, $D_k(\omega_i, \xi_i)$, ρ_{ukslj}, and ρ_{skisli} in the proposed FSI-MSRS method are changed due to the FSI effect. This section mainly investigates the variation of b_{ki}, ρ_{ukslj}, and ρ_{skislj} varying with the water depth of the side pier, where the incoherence effect (v_s/α=600 m/s) and wave passage effect (v_{app}=400 m/s) are considered.

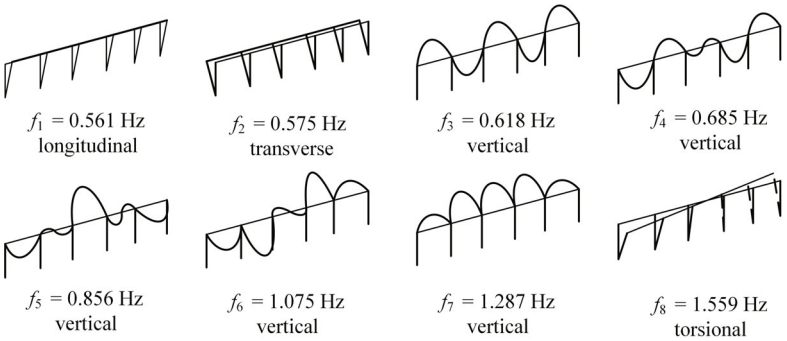

Fig. 3 First eight vibration modes of the bridge model

4.1 Effective modal participation factor

The effective modal participation factor (b_{ki}) depends on the ground motion at support k, vibration mode i, and the specific response of interest as stated in Section 2.2.1. The relative displacement between the top and bottom of the pier and the shearing force and bending moment at the bottom of the pier are calculated to investigate the b_{ki} varying with water depth, which is shown in Fig. 4.

In Fig. 4(a), the effective modal participation factor for displacement increases with water depth, and the side support increased more than the middle support. Figure 4(b) indicates that the b_{ki} for shearing force of the side supports changes slightly with water depth, while that of the middle supports decreases with water depth.

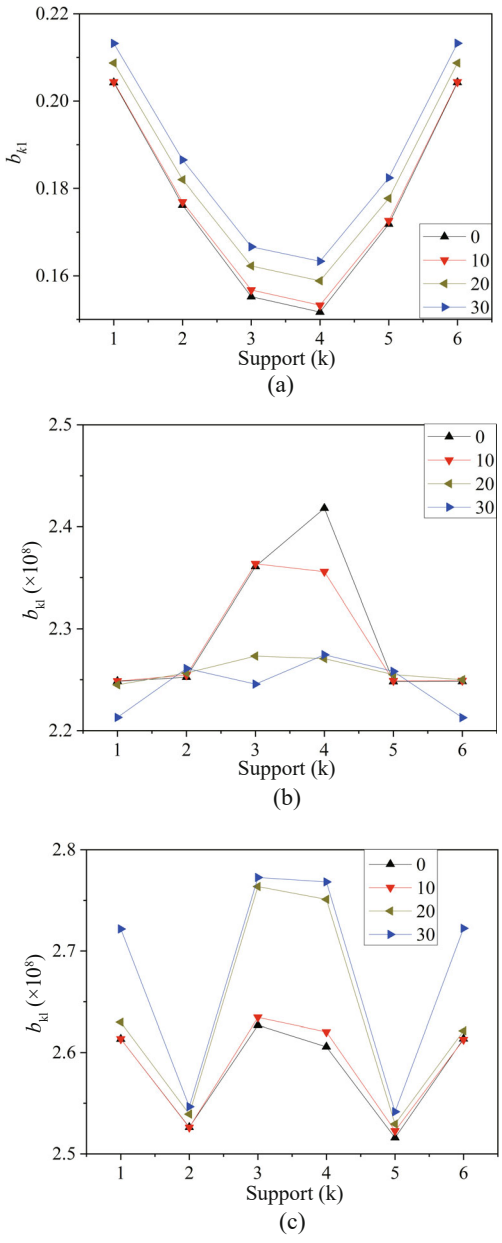

Fig. 4 Effective modal participation factor varying with water depth: (a) relative displacement; (b) shearing force; (c) bending moment

Figure 4(c) revealed that the b_{ki} for bending moment increases with water depth, and the change is smaller for supports 2 and 5 than that for the other supports. In general, the FSI effect has a certain influence on the effective modal participation factor with a maximum percentage of 8% as water depth changes from zero to 30 m.

4.2 Cross-correlation coefficient of ρ_{ukslj}

The influence of water depth on the cross-correlation coefficient of ρ_{ukslj} is shown in Fig. 5, when k=1 and j=1. Note that the results for the other values of k and j exhibit a similar behavior with the results here. Figure 5 shows that the ρ_{ukslj} increases with the water depth and the number of support l. The ρ_{ukslj} increases up to 24% as water depth changes from zero to 30 m, and the ρ_{ukslj} of support 6 can be 67% larger that of support 1. Therefore, the FSI effect significantly influence the ρ_{ukslj} and cannot be neglected.

4.3 Cross-correlation coefficient of ρ_{skislj}

The influence of water depth on the cross-correlation coefficient of ρ_{skislj} is shown in Fig. 6, when k = 3, i = 1, and j = 1. Note that the results for the other values of k, i, and j display a similar behavior with the results here. Figure 6 indicates that the cross-correlation coefficient ρ_{skislj} remains nearly unchanged at the different water

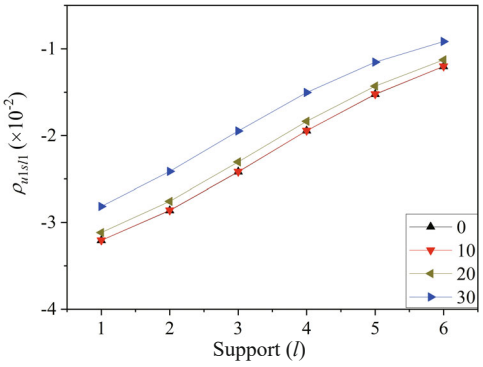

Fig. 5 Cross-correlation coefficient of ρ_{ukslj} varying with water depth

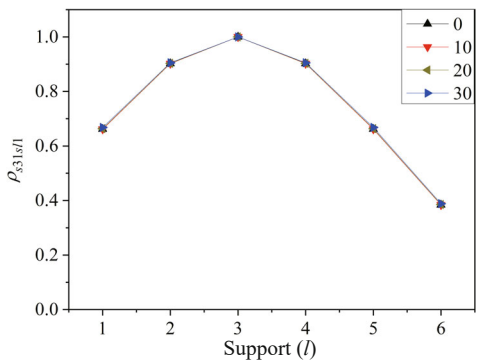

Fig. 6 Cross-correlation coefficient of ρ_{skislj} varying with water depth

depths, but increases when support l is close to support k. The coefficient decreases up to 61% when the ID of support l changes from 1 to 6. Therefore, the FSI effect has no influence on the cross-correlation coefficient of ρ_{skislj}.

5 Influence of GMSV and FSI effects on responses of bridge

5.1 Influence of incoherence effect

The relative displacement between the top and bottom of the pier (U_x), shearing force (V_x) and bending moment (M_y) at the bottom of the pier are calculated in this section. Figures 7 and 8 compare the mean peak values of the responses with different values of v_s/α that represents the incoherence effect, where Fig. 7 is for the results without water and Fig. 8 is for the results with water depth of 20 m.

As shown in Figs. 7 and 8, the responses decrease when the incoherence effect becomes stronger, and remain nearly unchanged when the v_s/α exceeds 2000 m/s. The ratio of the responses for $v_s/\alpha = \infty$ to those for $v_s/\alpha = 40$ can approximately be 4.0 for the relative displacement and 2.0 for shearing force and bending moment. Figure 7 indicates that the displacements of different piers are close to each other, the shearing force of pier 2 and pier 5 is smaller than that of other piers with a maximum percentage of 7%, and the bending moment of pier 2 and pier 5 is bigger than that of other piers with a maximum percentage of 20%. Figure 8 demonstrates that the FSI effect increases the relative displacements by approximately 7%, while it has little influence on the shearing force and bending moment. The exception is that the shearing force of pier 2 increases up to 15% and bending moment of pier 2 decreases up to 22% when considering the FSI effect. The reason may be that the hydrodynamic added mass caused by the FSI effect decreases the natural vibration frequencies of structure, which causes more modal contribution to the shearing force and less modal contribution to the bending moment of pier 2 than that of the other piers.

It can be concluded that the incoherence effect has a beneficial influence on the seismic responses of the bridge that it decreases the responses with a maximum percentage of 75%. This may be because the incoherence effect increases the pseudo-static component and decreases the dynamic component in Eq. (21), and the decrease exceeds the increase due to the existance of the dynamic amplification factor.

5.2 Influence of wave passage effect

The mean peak values of the responses with different values of v_{app} that represents the wave passage effect is shown in Figs. 9 and 10. Figure 9 shows the results that only consider the wave passage effect and Fig. 10 shows the results that consider the wave passage effect and FSI effect simultaneously with water depth of 20 m.

Figures 9 and 10 stated that the relative displacement, shearing force, and bending moment increase with

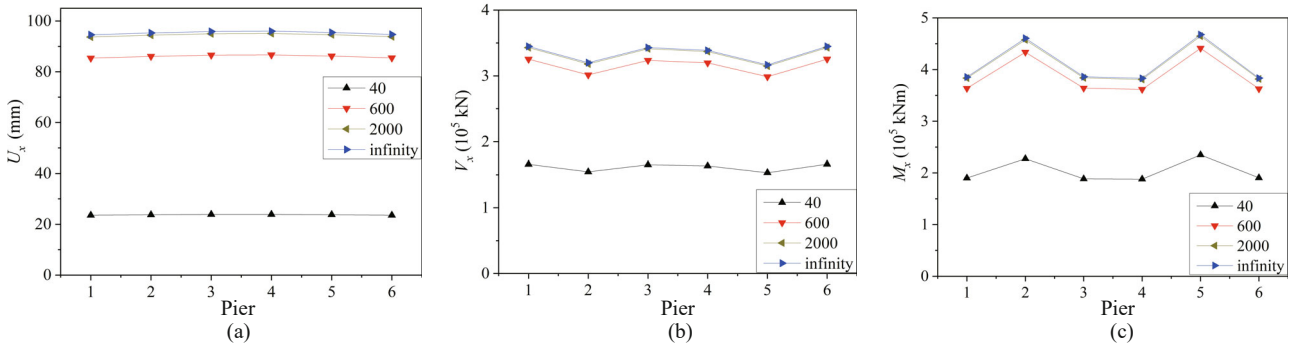

Fig. 7 Mean peak responses varying with v_s/α (h = 0): (a) relative displacement; (b) shearing force; (c) bending moment

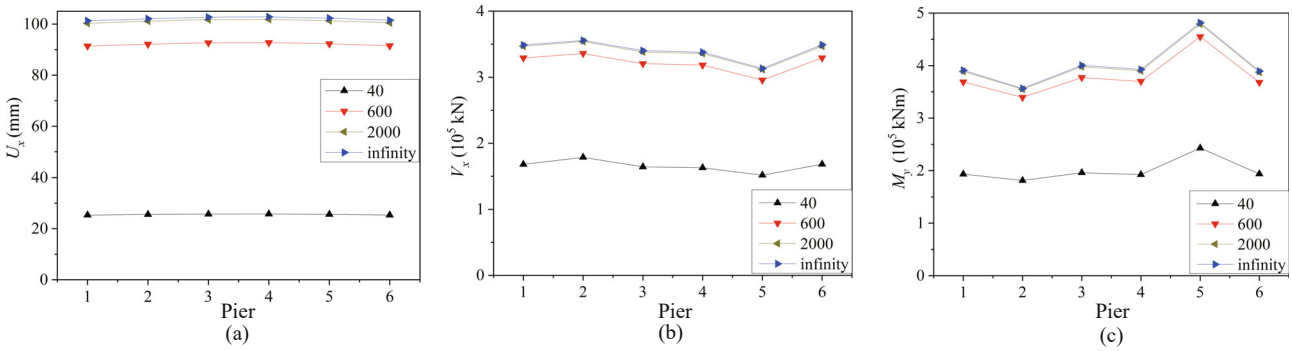

Fig. 8 Mean peak responses varying with v_s/α (h = 20 m): (a) relative displacement; (b) shearing force; (c) bending moment

increase of the surface apparent wave velocity, which means the wave passage effect becomes weak. The responses are not changed when the v_{app} exceeds 2000 m/s. In some extreme cases, such as v_{app}=40 m/s, the responses show a significant decrease, especially the relative displacement that is close to zero. The shearing force for v_{app} exceeds 2000 m/s and can be 7.0 times larger than that for v_{app} of 40 m/s, and the shearing force for v_{app} exceeds 2000 m/s, which can be 6.0 times larger than that for v_{app} of 40 m/s. Comparing the results without water with that considering the FSI effect, it can be observed that FSI effect increases the relative displacements by approximately 7%, while it has little influence on the shearing force and bending moment. The same exception is found in pier 2; the shearing force of pier 2 increases up to 53% and its bending moment decreases up to 34% when considering the FSI effect. The reason is same as that stated in Section 5.1.

Therefore, the wave passage effect has a similar effect with the incoherency effect analyzed in Section 5.1. It can decrease the seismic responses of the bridge up to 86%.

5.3 Influence of FSI effect

Four cases are considered when studying the influence of the FSI effect. Case 1 considers the FSI effect and uniform support motion. Case 2 considers the FSI effect and incoherence effect with v_s/α=600 m/s. Case 3 considers the FSI effect and wave passage effect with v_{app}=400 m/s. Case 4 considers the FSI effect, incoherence effect with v_s/α=600 m/s, and wave passage effect with v_{app}=400 m/s. Figures 11–14 show the results of the four cases. Table 3 lists the values of the various responses of piers 1-3. The following can be observed:

(1) The relative displacements increase with water depth. The reason is that the water increases the inertia force of the bridge, which then acts as added mass on the pier. There is little variation between displacements of different piers. For instance, the relative displacements of different piers in case 1 are approximately 128 mm when h = 0, while it is 129 mm, 136 mm, and 145 mm for h = 10 m, 20 m, and 30 m, respectively. FSI effect increases the relative displacement by approximately 1%, 7%, and 14% when water depth is 10 m, 20 m, and 30 m, respectively. The relative displacement decreases when considering the incoherence or wave passage effect. Therefore, the relative displacements in case 1 is the biggest, which is 18%, 25%, and 32% larger than those in case 2, case 3, and case 4, respectively.

(2) FSI effect has little influence on shearing force, except for pier 2, which increases up to 14%. The shearing forces of pier 2 and 5 are 7%–10% less than those of other piers. The incoherence effect and wave passage effect decrease shearing force. For example, the shearing forces of pier 1 in case 1 are around 4.0×10^5 kN, while it is 3.6×10^5 kN, 3.5×10^5 kN, and 3.3×10^5 kN in cases 2, 3, and 4, respectively. The shearing forces in case 2, 3, and 4 approximately decrease by 11%, 15%, and 20%, respectively, when compared with that in case 1.

(3) The bending moments slightly increase with water depth with a maximum percentage of 12%. The

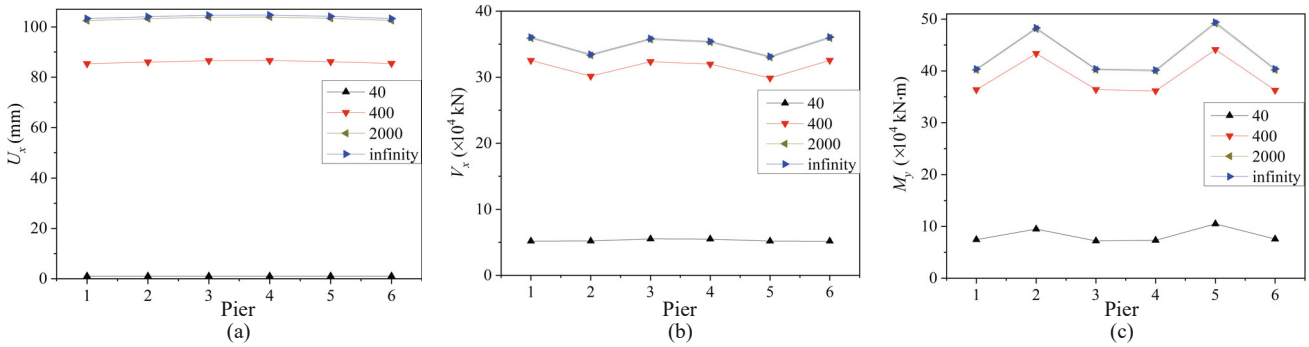

Fig. 9 Mean peak responses varying with v_{app} (h = 0): (a) relative displacement; (b) shearing force; (c) bending moment

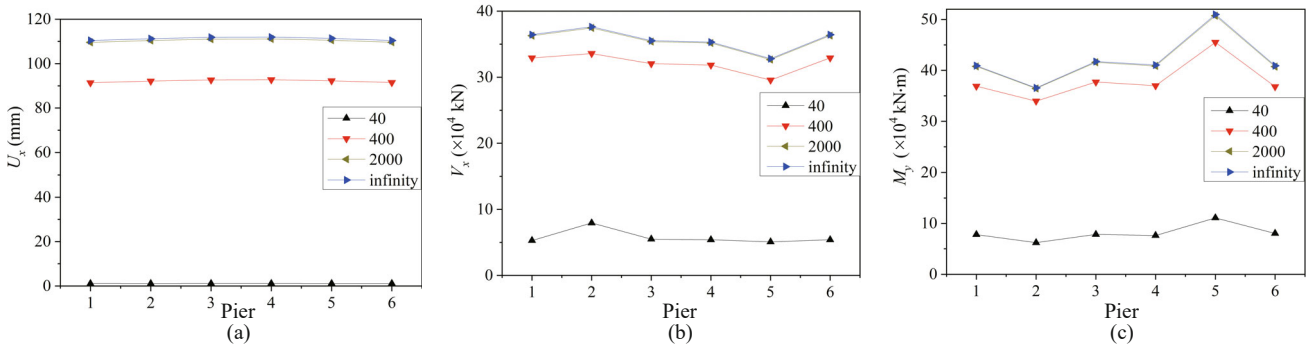

Fig. 10 Mean peak responses varying with v_{app} (h = 20 m): (a) relative displacement; (b) shearing force; (c) bending moment

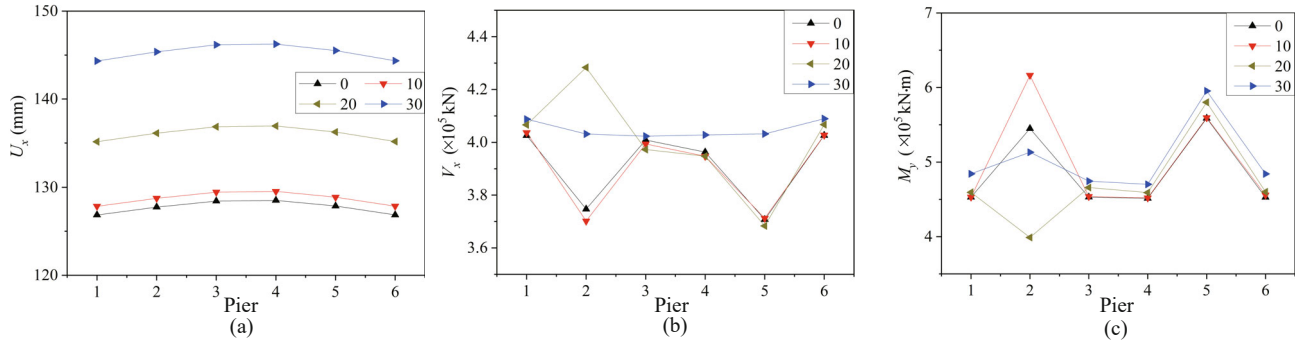

Fig. 11 Mean peak responses varying with water depth (v_s/α = infinity, v_{app} = infinity): (a) relative displacement; (b) shearing force; (c) bending moment

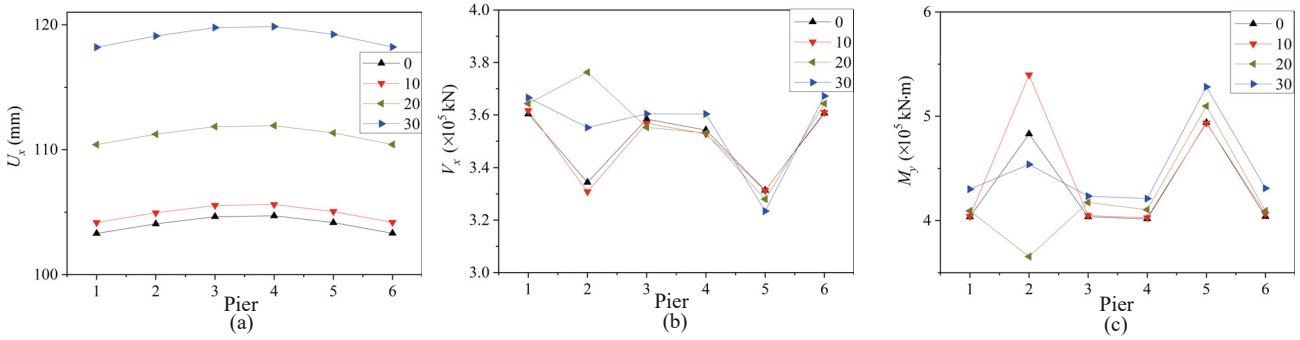

Fig. 12 Mean peak responses varying with water depth (v_s/α = 600 m/s, v_{app} = infinity): (a) relative displacement; (b) shearing force; (c) bending moment

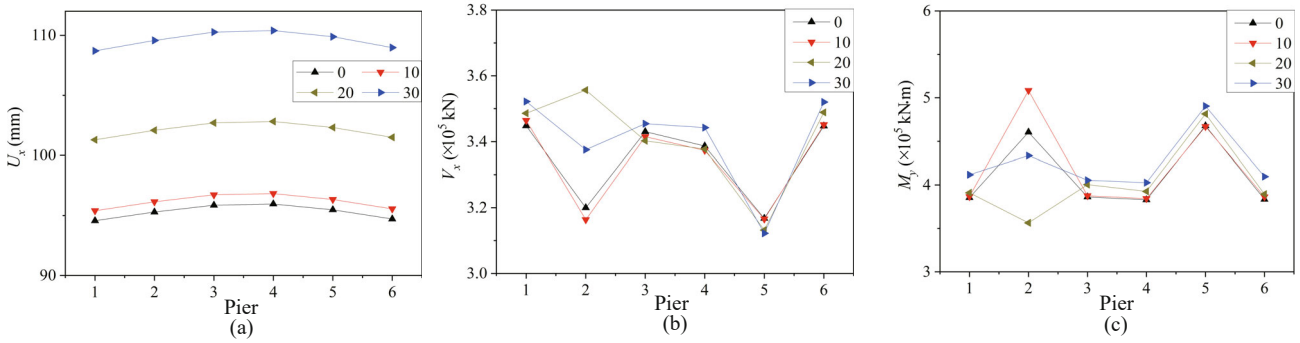

Fig. 13 Mean peak responses varying with water depth (v_s/α = infinity, v_{app} = 400 m/s): (a) relative displacement; (b) shearing force; (c) bending moment

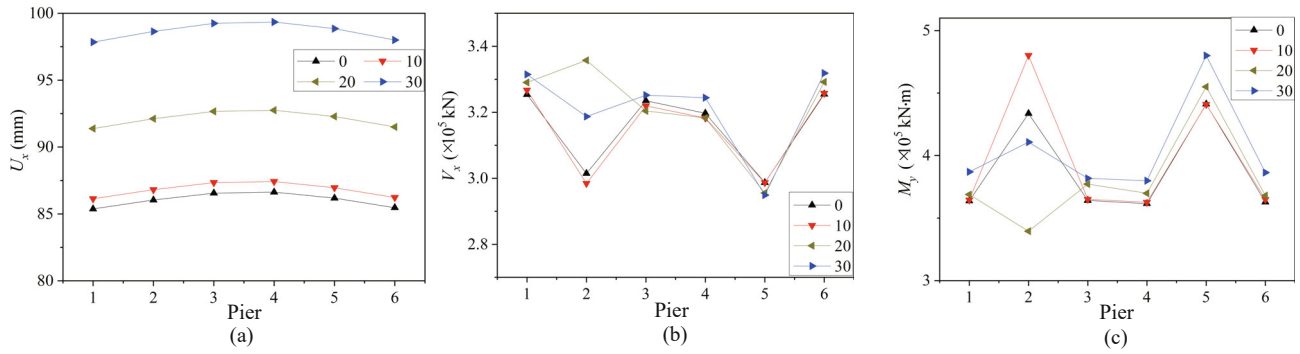

Fig. 14 Mean peak responses varying with water depth (v_s/α = 600 m/s, v_{app} = 400 m/s): (a) relative displacement; (b) shearing force; (c) bending moment

Table 3 Specific values of the various responses of piers 1-3

Case number		Relative displacement (mm)				Shearing force ($\times10^5$ kN)				Bending moment ($\times10^5$ kN·m)			
		0	10	20	30	0	10	20	30	0	10	20	30
Pier 1	1	126.8	127.8	135.1	144.3	4.02	4.04	4.07	4.09	4.53	4.53	4.59	4.84
	2	103.3	104.2	110.4	118.2	3.60	3.62	3.64	3.67	4.03	4.04	4.09	4.30
	3	94.6	95.4	101.3	108.7	3.45	3.46	3.49	3.52	3.85	3.87	3.91	4.12
	4	85.4	86.1	91.4	97.8	3.25	3.27	3.29	3.31	3.64	3.64	3.69	3.87
Pier 2	1	127.8	128.7	136.1	145.4	3.75	3.70	4.28	4.03	5.45	6.16	3.99	5.13
	2	104.7	105.0	111.2	119.1	3.34	3.31	3.76	3.55	4.83	5.40	3.65	4.54
	3	95.3	96.1	102.1	109.6	3.20	3.16	3.56	3.37	4.60	5.08	3.56	4.33
	4	86.0	86.8	92.1	98.6	3.01	2.98	3.36	3.19	4.34	4.80	3.39	4.11
Pier 3	1	128.4	129.4	136.8	146.2	4.01	3.99	3.97	4.02	4.53	4.54	4.66	4.74
	2	104.6	105.5	111.9	119.8	3.58	3.57	3.55	3.60	4.04	4.05	4.17	4.23
	3	95.9	96.7	102.7	110.4	3.43	3.41	3.40	3.45	3.86	3.88	4.00	4.05
	4	86.5	87.3	92.7	99.3	3.23	3.22	3.20	3.25	3.64	3.65	3.77	3.82

bending moments of pier 2 and 5 are 19%–26% larger than those of the other piers. The bending moment decreases when considering the incoherence effect or wave passage effect. Taking the shearing force of pier 1 as an example, the shearing forces are around 4.6×10^5 kN·m, 4.1×10^5 kN·m, 3.9×10^5 kN·m, and 3.7×10^5 kN·m when considering uniform support motion, incoherence effect, wave passage effect, and incoherence and wave passage effects, respectively. The bending moment in cases 2, 3, and 4 approximately decrease by 11%, 15%, and 20%, respectively, when compared with that in case 1.

In addition, the responses of bridges considering combined effects of FSI and incoherence or wave passage is not the simple superposition of that considering the individual effect. For instance, the relative displacement of pier 2 in case 1 is 127.8 mm without water and 145.4 mm with water depth of 30 m, which increases 17.6 mm caused by the FSI effect. The relative displacement of pier 2 in case 2 is 104.7 mm without water and 119.1 mm with water depth of 30 m, which decreases 23.1 mm caused by the incoherence effect and decreases 8.7 mm caused by the coupling effect of FSI and incoherence, and 8.7 is not the difference between 23.1 and 17.6. A similar conclusion can be obtained for the responses of bridges considering that the coupling effect of incoherence and wave passage is not the simple superposition of that considering the individual effect.

6 Conclusions

Based on the radiation wave theory, the original MSRS method is extended to consider the FSI effect for seismic analysis of bridges in deep water, called the FSI-MSRS method. The method is then verified by comparison with the results in the reference (Der Kiureghian and Neuenhofer, 1992). The influence of FSI effect on the related coefficients is investigated. Finally, a five-span steel-concrete continuous beam bridge is adopted to examine the influence of the GMSV effect and FSI effect on seismic responses of the bridge. The following conclusions are drawn:

(1) The effective modal participation factor (b_{ki}) slightly increases with water depth with a maximum percentage of 8%. The cross-correlation coefficient of ρ_{ukslj} increases with water depth with a maximum percentage of 24%. The cross-correlation coefficients of ρ_{skisli} remains unchanged at the different water depths.

(2) FSI effect and GMSV effect have the opposite influence on the seismic responses of the bridge. The incoherence effect decreases the responses up to 75%, the wave passage effect decreases the responses up to 86%, and the FSI effect increases the responses up to 26%. The three effects need to be considered in the seismic design of deep-water bridges.

(3) The responses of bridges considering the coupling effect of FSI and incoherence or wave passage is not the simple superposition of that considering the individual effect. And the responses of bridges considering the coupling effect of incoherence and wave passage is not the simple superposition of that considering the individual effect.

In general, the proposed FSI-MSRS method can be used to study the seismic responses of deep-water bridges considering the GMSV effect and FSI effect simultaneously. The method can be extended to investigate the performance of bridges subjected to multi-dimensional earthquake excitations coupled with certain other excitations, such as waves or ocean currents.

Acknowledgment

The authors gratefully acknowledge the support for this research provided by the National Natural

Science Foundation of China (Grant Nos. 51427901 and 51678407), Tianjin Municipal Education Commission (Grant No. 2021KJ055), and Fundamental Research Funds for the Central Universities of China (Grant No. 2000560616).

References

Abdel SE, Hayashikawa T and Dorka U (2011), "Ground Motion Spatial Variability Effects on Seismic Response Control of Cable-Stayed Bridges," *Earthquake Engineering and Engineering Vibration*, **10**(1): 37–49.

Avilés J and Li X (2001), "Hydrodynamic Pressures on Axisymmetric Offshore Structures Considering Seabed Flexibility," *Computers and Structures*, **79**(29): 2595–2606.

Bi KM, Hao H and Chouw N (2010), "Influence of Ground Motion Spatial Variation, Site Condition and SSI on the Required Separation Distances of Bridge Structures to Avoid Seismic Pounding," *Earthquake Engineering and Structural Dynamics*, **40**(9): 1027–1043.

Cai SQ, Long XM and Gan ZJ (2003), "A Method to Estimate the Forces Exerted by Internal Solitons on Cylindrical Piles," *Ocean Engineering*, **30**(5): 673–689.

Chopra A and Goyal A (1991), "Simplified Earthquake Analysis of Intake-Outlet Towers," *Journal of Structural Engineering*, **117**(3): 767–788.

Clough RW and Penzien J (1975), *Dynamics of Structures*, McGrawHill, New York.

Der Kiureghian A and Neuenhofer A (1992), "Response Spectrum Method for Multi-Support Seismic Excitations," *Earthquake Engineering and Structural Dynamics*, **21**(8): 713–740.

Ding Y, Ma R, Shi YD, *et al*. (2018), "Underwater Shaking Table Tests on Bridge Pier under Combined Earthquake and Wave-Current Action," *Marine Structures*, **58**(15): 301–320.

Dumanogluid AA and Soyluk K (2003), "A Stochastic Analysis of Long Span Structures Subjected to Spatially Varying Ground Motions Including the Site-Response Effect," *Engineering Structures*, **25**(10): 1301–1310.

Gu Q and Huang SR (2017), *Practical Manual for OpenSees Software*, Science Press, Beijing, China. (in Chinese)

Hu L, Xu YL and Zheng Y (2012), "Conditional Simulation of Spatially Variable Seismic Ground Motions Based on Evolutionary Spectra," *Earthquake Engineering and Structural Dynamics*, **41**(15): 2125–2139.

Huang X (2011), *Mechanism of Water-Bridge Pier Dynamic Interaction and Nonlinear Seismic Responses of Bridges in Deep Water*, Tianjin University, Tianjin, China. (in Chinese)

Konakli K and Der Kiureghian A (2011), "Extended MSRS Rule for Seismic Analysis of Bridges Subjected to Differential Support Motions," *Earthquake Engineering and Structural Dynamics*, **40**(12): 1315–1335.

Koufoudi E, Chaljub E, Dufour F, *et al*. (2018), "Spatial Variability of Earthquake Ground Motions at the Dam–Foundation Rock Interface of Saint Guérin: Experimental and Numerical Investigations," *Bulletin of Earthquake Engineering*, **16**(5): 1751–1777.

Li MG, Li X and Zhou J (2010), "A Modified Method for Simulating Non-Stationary Multi-Point Earthquake Ground Motion," *Earthquake Engineering and Engineering Vibration*, **9**(2): 201–211.

Li Q and Yang WL (2013), "An Improved Method of Hydrodynamic Pressure Calculation for Circular Hollow Piers in Deep Water Under Earthquake," *Ocean Engineering*, **72**: 241–256.

Li X, Zhang DY, Yan WM, *et al*. (2015), "Shake-Table Test for a Typical Curved Bridge: Wave Passage and Local Site Effects," *Journal of Bridge Engineering*, **20**(2): 04014061.

Li YC and Di QS (2011), "Numerical Simulation of Dynamic Characteristics of a Cable-Stayed Aqueduct Bridge," *Earthquake Engineering and Engineering Vibration*, **10**(4): 569–579.

Li ZX, Wu K, Shi YD, *et al*. (2019), "Experimental Study on the Interaction Between Water and Cylindrical Structure Under Earthquake Action," *Ocean Engineering*, **188**: 106330.

Lin JH, Zhang YH and Zhao Y (2005), "Seismic Spatial Effects on Long-Span Bridge Response in Nonstationary Inhomogeneous Random Fields," *Earthquake Engineering and Engineering Vibration*, **4**(1): 75–82.

Meng SB, Ding Y and Zhu HT (2018), "Stochastic Response of a Coastal Cable-Stayed Bridge Subjected to Correlated Wind and Waves," *Journal of Bridge Engineering*, **23**(12): 04018091.

Miao YJ, Chen XJ, Ye YL, *et al*. (2021), "Numerical Modeling and Dynamic Analysis of a Floating Bridge Subjected to Wind, Wave and Current Loads," *Journal of Offshore Mechanics and Arctic Engineering*, **141**(1): 011601.

Mirzabozorg H, Akbari M and Ardebili MA (2012), "Wave Passage and Incoherency Effects on Seismic Response of High Arch Dams," *Earthquake Engineering and Engineering Vibration*, **11**(4): 567–578.

Mohammadnezhad H, Ghaemian M and Noorzad A (2019), "Seismic Analysis of Dam-Foundation-Reservoir System Including the Effects of Foundation Mass and Radiation Damping," *Earthquake Engineering and Engineering Vibration*, **18**(1): 203–218.

Morison J, Johnson J and Schaaf S (1950), "The Force Exerted by Surface Waves on Piles," *Journal of Petroleum Technology*, **2**(5): 149–154.

Nakanura Y, Der Kiureghian A and Liu D (1993), "Multiple-Support Response Spectrum Analysis of the Golden Gate Bridge," *Report No. UCB/EERC-93/05*, Earthquake Engineering Research Center, University of California, Berkeley.

Nakasone Y, Yoshimoto S and Stolarski TA (2006), *Engineering Analysis with ANSYS Software*, Elsevier, Amsterdam, Netherlands.

Nazarov ZP and Poznyak E (2018), "Response Spectrum Method for Integrated and Differential Spatial Seismic Ground Motions," *Soil Dynamics and Earthquake Engineering*, **108**: 69–78.

Penzien J and Kaul M (1972), "Response of Offshore Towers to Strong Motion Earthquakes," *Earthquake Engineering and Structural Dynamics*, **1**(1): 55–68.

Penzien J, Kaul M and Berge B (1972), "Stochastic Response of Offshore Towers to Random Sea Waves and Strong Motion Earthquakes," *Computers and Structures*, **2**(5-6): 733–756.

Song B, Zheng F and Li Y (2013), "Study on a Simplified Calculation Method for Hydrodynamic Pressure to Slender Structures Under Earthquakes," *Journal of Earthquake Engineering*, **17**(5): 720–735.

Soyluk K and Dumanoglu A (2004), "Spatial Variability Effects of Ground Motions on Cable-Stayed Bridges," *Soil Dynamics and Earthquake Engineering*, **24**(3): 241–-250.

Sun K and Nogami T (1991), "Earthquake Induced Hydrodynamic Pressure on Axisymmetric Offshore Structures," *Earthquake Engineering and Structural Dynamics*, **20**(5): 429–440.

Veletsos AS, Prasad AM and Hahn G (2010), "Fluid-structure Interaction Effects for Offshore Structures," *Earthquake Engineering and Structural Dynamics*, **16**(5): 631–652.

Wang H, Wu YF, Sha B, *et al*. (2018), "Compositive Optimal Control for the Seismic Response of a Long-Span Triple-Tower Suspension Bridge," *International Journal of Structural Stability and Dynamics*, **18**(8): 1840009.

Wang ZH, Gu CS and Chen GX (2011), "Seismic Response of Bridge Pier in Deep Water Considering Close Fluid-Structure Interaction Effects," *Advanced Materials Research*, **243-249**: 1803–1810.

Wang ZQ and Der Kiureghian A (2014), "Multiple-Support Response Spectrum Analysis Using Load-Dependent Ritz Vectors," *Earthquake Engineering and Structural Dynamics*, **43**(15): 2283–2297.

Wei K, Yuan WC and Bouaanani N (2013), "Experimental and Numerical Assessment of the Three-Dimensional Modal Dynamic Response of Bridge Pile Foundations Submerged in Water," *Journal of Bridge Engineering*, **18**(10): 1032–1041.

Wepf DH, Wolf JP and Bachmann H (1988), "Hydrodynamic-Stiffness Matrix Based on Boundary Elements for Time-Domain Dam-Reservoir-Soil Analysis," *Earthquake Engineering and Structural Dynamics*, **16**(3): 417–432.

Yang QS, Saiidi MS, Wang H, *et al*. (2002), "Influence of Earthquake Ground Motion Incoherency on Multi-Support Structures," *Earthquake Engineering and Engineering Vibration*, **1**(2): 167–180.

Yu RF and Zhou XY (2008), "Response Spectrum Analysis for Non-Classically Damped Linear System with Multiple-Support Excitations," *Bulletin of Earthquake Engineering*, **6**(2): 261–284.

Yuan ZD and Huang ZH (2010), "An Experimental Study of Inertia and Drag Coefficients for a Truncated Circular Cylinder in Regular Waves," *Journal of Hydrodynamics, Ser. B*, **22**(5): 318–323.

Zhang D, Li N, Li ZX, *et al*. (2020), "Seismic Performance of Bridge with Unbonded Posttensioned Self-Centering Segmented Concrete-Filled Steel-Tube Columns: An Underwater Shaking Table Test," *Soil Dynamic and Earthquake Engineering*, **138**: 106350.

Zheng WZ, Wang H, Li J, *et al*. (2019), "Parametric Study of SMA-Based Friction Pendulum System for Response Control of Bridges Under Near-Fault Ground Motions," *Journal of Earthquake Engineering*, **25**(8): 1494–1512.